Construction and Analysis of a Modified Nb_3Sn 11 T Short Dipole Model

Carmen Abad Cabrera, Diego Perini, Tavis Alexander Bampton, Oussama Id Bahmane, Susana Izquierdo Bermudez, Nicolas Bourcey, Arnaud Devred, *Senior Member, IEEE*, Ruth Diaz Vez, Cedric Garion, Michael Guinchard, Franco Julio Mangiarotti, Attilio Milanese, Marco Morrone, Sylvain Mugnier, Nicholas Lusa, Sebastien Luzieux, Francois-Olivier Pincot, Roland Piccin, Herve Prin, Frederic Savary, Giancarlo Spigo, and Gerard Willering

***Abstract*—The 5.2-m-long, 11 T double-aperture Nb_3Sn Dipole Magnet was designed to replace some of the standard, 15-m-long 8.3 T Nb–Ti main dipole magnets in the Large Hadron Collider. After the production and test of several of 2-m-long models, the test of full-length 11 T series magnets revealed signs of performance degradation in the coil ends after a sequence of electromagnetic and thermal cycles. The possible sources for performance degradation were categorized into two groups: issues internal to the coils and issues with the coil support structure, in particular in the magnet ends. To address the constraints external to the coil, two mitigation measures were proposed: (1) reducing peak stresses in the coil ends and (2) improving the coil end support and axial loading. To validate the mitigation measures, a double-aperture model magnet, MBHDP301, was designed, manufactured, and power tested. The magnet was manufactured with four available coils, three of which had been assembled and tested in previous magnets. Two new features were implemented in both apertures to reduce the peak stresses in the coil ends (mitigation measure 1). The first involved a change in material of the removable pole from titanium to austenitic stainless steel, while the second introduced a gradual reduction of prestress applied in the ends of the coil straight section. For one of the two apertures, in addition, an end cage system was installed to improve coil end support and axial loading (mitigation measure 2). The two apertures in the magnet can be independently powered, facilitating comparison studies. This paper describes the manufacturing, mechanical measurements analysis and cold powering test campaign results of the MBHDP301 model magnet. The lessons learned from this work can be useful and directly applicable to future cosθ high field dipole magnets.**

***Index Terms*—Accelerator magnets, High field, HL-LHC, Nb_3Sn.**

I. Introduction

THE high luminosity upgrade of the Large Hadron Collider (HL-LHC) project at CERN planned to replace some 15-m-long, 8.3 T Nb–Ti LHC dipole magnets by shorter, 5.2-m-long, 11 T units, providing the same integrated bend strength but opening space for additional collimators [1]. To this end, a magnet development program was initiated circa 2010, first in collaboration with Fermilab, then at CERN where nine 11 T short model magnets were manufactured and tested and six of them reached ultimate current at 1.9 K [2]. However, this performance has not been reproduced in the long magnets. Four 11 T series magnets were tested. While the first magnet (S1) reached nominal current after a few training quenches and exhibited good training memory after thermal cycling, the subsequent three magnets showed performance degradation either after the first cooldown (S3) or after two or more cooldowns (S2 and S4). The quenches in S2 and S4 were localized primarily in the coil heads, which were interpreted as local conductor degradation. These results led to the decision at the end of 2021 not to install the 11 T magnets during Long Shutdown 2 (LS2) and to reassess the next steps.

A Task Force was set up in order to review the situation and determine possible corrective actions. The Task Force included three main actions: disassembly an autopsy of S2, S3 and S4, metallographic analyses of coil sections where quenches had been localized [3] and the development of a new 3D finite element analysis model [4]. The main finding of the metallographic analyses and of the FE simulations [4] was the presence of high stress areas in the coil ends, corresponding to the quench localizations.

In particular, tomographic analysis showed pop-out strands at the exit of the coil ends [3]. Two types of issues were identified, internal and external to the coils. The coil manufacturing issues cannot be addressed without manufacturing new coils, which is outside of the scope of this study. The external issues identified are (see Fig. 1):

- High-stress areas and stress singularities after collaring in the coil head outer layer's first turn.
- High-stress areas and stress singularities after cooldown in the coil head outer layer's first turn.
- High peak stresses during powering in the coil head pole turn.
- Non-optimal coil end support for the electromagnetic axial force difference in between the coil head turns.
- Non-optimal axial loading. S2 and S3 cold masses had a loosened and deformed axial loading screw (bullet).

The main objective of this work is to implement different features in a 2-m-long, 11 T magnet, MBHDP301, with two

Received 24 September 2024; revised 18 November 2024; accepted 6 December 2024. Date of publication 1 January 2025; date of current version 20 January 2025. *(Corresponding author: Carmen Abad Cabrera.)*

The authors are with CERN, CH-1211 Geneva, Switzerland (e-mail: carmen.abad.cabrera@cern.ch).

Color versions of one or more figures in this article are available at https://doi.org/10.1109/TASC.2024.3519076.

Digital Object Identifier 10.1109/TASC.2024.3519076

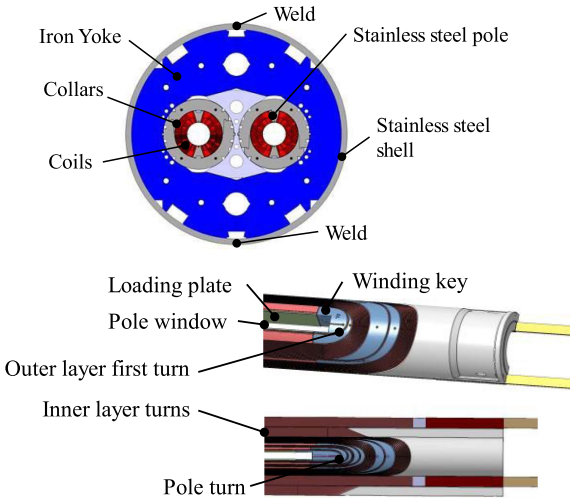

Fig. 1. 11 T 2 in 1 magnet cross section (top) and detailed view of the two layers 11 T impregnated coil (bottom).

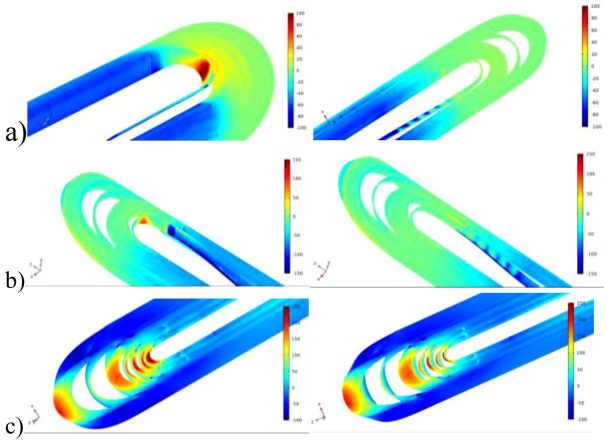

Fig. 2. Stress distribution (MPa) in the coil head windings before (left) and after (right) the mitigation measures 1. (a) Azimuthal stress in outer layer turns after collaring; (b) Azimuthal stress in outer layer turns after cooldown; (c) Axial stress in inner layer turns during powering. FEA simulations only represent the connection side head.

different configuration apertures SP301 and SP302, to compare these apertures mechanically, with previous magnets and with the FEA results. The interconnection between the coils allows for individual powering of each aperture, as well as their double powering.

II. Mitigation Measures

A. Mitigation Measures 1

The coil is prestressed by introducing excess in the assembly through shims placed between the removable pole and the coil loading plate. It has been noticed that in the previous 11 T configuration, there is a sudden change in excess at the transition from the loading plate to the coil winding key (see Fig. 1). The aim is to mitigate this abrupt change by reducing the excess at the end of the straight section. According to the FEA model [4], this excess reduction at the ends reduces the azimuthal peak stress from 120 MPa (Fig. 2(a) left) to 10 MPa (Fig. 2(a) right) in the first turn of the outer layer and mitigates the stress singularities at the connection between the coil winding key and the loading plate during collaring.

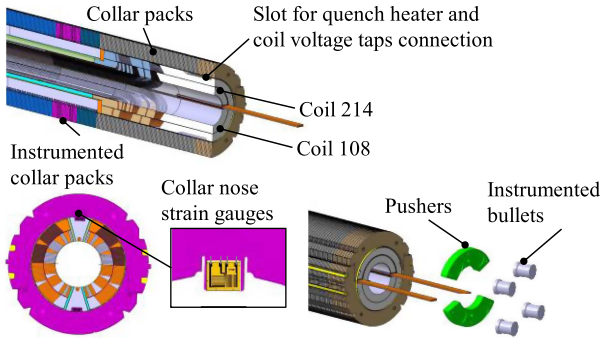

Fig. 3. Configuration of collared coil SP301, as seen from the from the connection side end.

The reduction of the high-stress areas in the coil ends after the cooldown phase is addressed by changing the material of the removable pole from titanium to 316LN stainless steel, which has a thermal contraction similar to that of the coil. The thermal contraction from 300 K to 4 K is 1.7 mm/m for titanium, 2.95 mm/m for austenitic stainless steel, and estimated to be 2.78 mm/m for the homogenized coil. With this change, after cooldown, the azimuthal peak stress in the outer layer first turn decreases from 95 MPa (Fig. 2(b) left) to −20 MPa (Fig. 2(b) right) and the tensile stress singularity that occurred at the tip of the copper wedges and at the level of the junction between the winding key and the loading plate disappears.

These two solutions aim at reducing the peak stresses during powering, but they remain critical. The axial peak stress in the first turn of the inner layer is reduced from 310 MPa (Fig. 2(c) left) to 250 MPa (Fig. 2(c) right). These new features are first implemented in the collared coil, referred to as SP301. The axial loading and support are provided by one pusher and two bullets per coil, as illustrated in Fig. 3.

B. Mitigation Measures 2

In the other aperture, SP302, the same mitigation measures as in mitigation 1 were implemented. Additionally, a new end cage system was installed with the aim of enhancing the support for the coil ends and axial loading. The end cage, depicted in Fig. 4, applies preload to the coil heads, using three rods per coil, during assembly and aims to hold them in place during powering. This is intended to limit and possibly eliminate misplacements between the head turns due to differences in axial electromagnetic forces. According to the 3D FEA model [4], the addition of the end cage did not result in significant stress reduction in the coil heads. However, a drawback was identified: during powering, the inner layer mid-plane area at the level of the end cage experiences an increase in compression stress due to the massive collar and the axial pre-load of the end cage, as shown in Fig. 5. Mid-plane stresses higher than −150 MPa have been found a performance degradation in the coils in previous magnets [2] and stresses higher than −175 MPa in cable samples [5]. Despite this

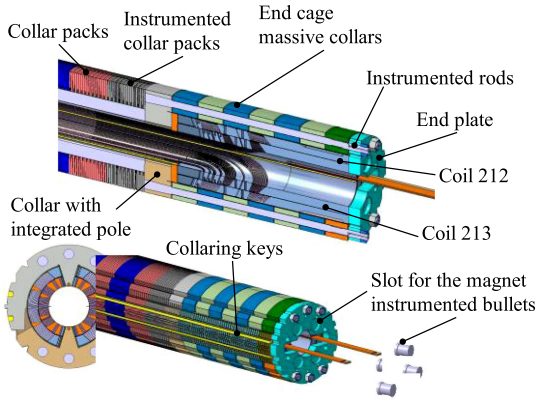

Fig. 4. Configuration of collared coil SP302, as seen from the from the connection side end.

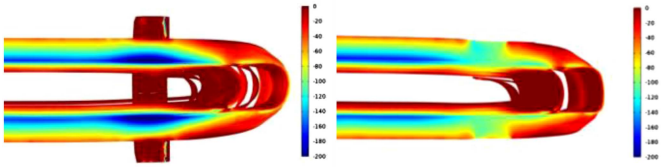

Fig. 5. Azimuthal stresses (MPa) in the coil inner layer mid-plane during powering in SP302 with the end cage prestressed (left) and with the end cage with zero prestress (right).

disadvantage, the cage was implemented based on its successful use in previous NbTi magnets (FRESCA [6] and MFISC [7]).

III. Magnet Configuration and Fabrication

The magnet fabrication process consists of first locking two coils into the collars' closed cavity, forming the so-called collared coil. This is followed by assembling the two collared coils into the yoke and finishes with the longitudinal welding of the two halve shells (Fig. 1).

A. Mechanical Instrumentation

To understand the behavior of the magnet during assembly and powering, a comprehensive instrumentation plan was developed. Six cross sections, two at the connection side end, two in the middle, and two at the non-connection side end were instrumented with strain gauges on the collar nose (showed in Fig. 3) in a half-bridge configuration with Poisson ratio compensation to measure the compression strain in the collar nose [8]. Twelve rods in the end cage (Fig. 4) in SP302 were instrumented with full-bridge gauges and Poisson ratio compensation to measure the normal strain. Additionally, sixteen bullet gauges, based on full-bridge configurations with Poisson ratio compensation, were located between the coils and the magnet end plate (as shown in Figs. 3 and 4) at each extremity for both apertures to measure strain in the bullets. This setup aimed to calculate the force exerted by the coil against the magnet end plates.

B. Coils

The four Nb_3Sn impregnated coils used in the MBHDP301 magnet are as follows: coil 108 is made from the first-generation RRP (Rod Restack Process) type strand with a keystone angle of 0.79°, while coils 212, 213, and 214 are made from the second-generation PIT (Powder In Tube) cable with a keystone angle of 0.50° [9]. Coil 108 has been used in two collared coils before, CC102 in model magnets SP102 and DP101 [2] and after CC999, which was used for a mechanical test. Coils 212 and 213 formed the collared coil CC202 in magnet DP201 [10]. Coil 214 is the only virgin coil (not assembled and not power tested) available. The collaring parameters of these coils in previous magnets and in the magnet DP301 are listed in Table I. Aperture 1 (SP301) is composed by the coil 108 and 214 while aperture 2 (SP302) by coil 212 and 213.

TABLE I
Collaring Parameters in the Collared Coils of the Reused Coil for the Magnet MBHDP301

Parameter	Unit	Collared coil											
		CC102		CC999		CC202		CC301(1)		CC301(2)		CC302	
		106	108	106	108	212	213	108	214	108	214	212	213
Collaring													
Nominal collaring cavity	mm	70		70		70		70		70		70	
Stoppers height with shims	mm	70.1		69.85		69.85		69.85		69.85		69.85	
Key clearance	um	-100		150		150		150		151		150	
Collaring force	MN	34.0		8.5		6.0		5.4		5.4		6.6	
Collar nose stress													
at max collaring force	MPa	-227		-		-86		-164		-103		-161	
after key insertion	MPa	-186		-		-46		-134		-65		-130	

(1) Collaring for Test 1
(2) Collaring for Test 2

C. Shimming Plan

A new shimming plan with excess reduction in the ends of the coil straight section is designed and implemented. The reused coils 108, 212 and 213 were measured and analyze according to [11]. Measurements after impregnation and after cold test were compared. This comparison revealed that, after the cold test, the coil outer radius increased by an average of 0.1 mm and the coil azimuthal size decreased by an average of 0.06 mm. Considering that the prestress is applied azimuthally, measurements of the virgin coil were used for conservative shim calculations. The shims were manufactured in austenitic stainless steel, with their thickness gradually changing along the straight section in steps of 0.025 mm. The target quadrant excess in the coil straight section was set at an upper limit of 0.3 mm which was determined earlier to prevent coil overstressing [8]. Collaring tests, with pressure sensitive films placed between the coils' mid-planes verified the stress reduction amplitude in the ends of the coil's straight section. The resulting average excess in the middle was 0.220 mm in SP301 and 0.210 mm in SP302, with an excess reduction until approximately 0.075 mm in the last 150 mm, as depicted in Fig. 6. The collaring procedure developed in [8] was followed, with forces of 5.4 MN applied for SP301 and 6.6 MN for SP302, as indicated in Table I. The objective was to achieve an average stress of −55 MPa in the coil mid-plane, according to [8] the stress in the collar nose is about twice the average coil mid-plane stress, leading to a target of −110 MPa in the collars. The achieved collar prestress was −134 MPa in SP301 and −130 MPa in SP302 in the central sections.

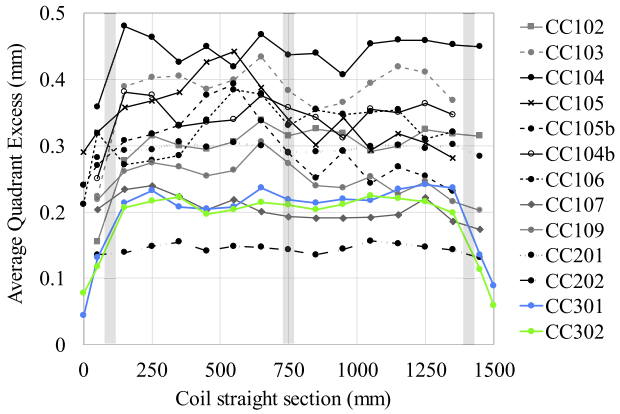

Fig. 6. Average quadrant excess with shim in all the 11 T model collared coils, the shadow represents the sections with the collars instrumented with strain gauges.

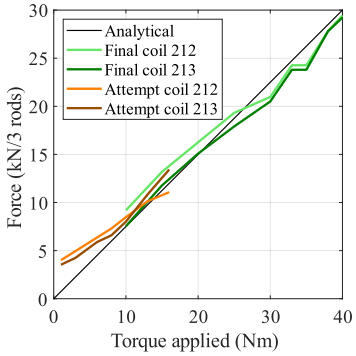

Fig. 7. Force in three rods vs torque applied during the initial attempt of end cage loading and final loading at the non-connection side head.

D. Coil Head Support and Axial Loading

The coil heads of aperture SP302 are loaded after collaring by means of the end cage system. The preload applied by the end cage is 12% of the axial electromagnetic forces, which are 470 kN per aperture at nominal current, resulting in a preload of 56.4 kN per collared coil.

As depicted in Fig. 4, the end cage consists of a massive collar with an integrated pole, massive collars acting as fillers, an end plate, all made from 304L stainless steel, with six rods made from 316LN stainless steel connecting the end plate to the first collar. Proper alignment of the top and bottom coil pole windows (Fig. 1) and ensuring both coil heads are of the same length are crucial for a correct end cage loading and operation. The coil heads nominal length is 295.5 mm for the connection side and 178 mm for the non-connection side.

During the loading process, the torque applied to the rods is gradually increased. In the initial attempt of end cage loading, an offset was observed on the non-connection side between the two coils, 212 and 213. Fig. 7 represents the torque against the force in the non-connection side rods of coil 212 (in orange) and coil 213 (in brown). After applying 10 Nm of torque, the curves intersect and cross, indicating that the applied force is increasingly transmitted to coil 213, suggesting a misalignment of the coils. The collared coil was then disassembled, and the misalignment was corrected. The green curves in Fig. 7 represent the final loading condition, where both coils are loaded uniformly. The torque analytical calculation is detailed in (1), where F is the tension force in the rod, Φ is the diameter of the rod (10 mm in the area where the strain gauges are located and 12 mm in the rest of the rod length) and 0.4 is the nut factor. The rods are subsequently fixed in position with screw nuts and welded.

$$T_{rod} = 0.4 F_{rod} \Phi_{rod} \tag{1}$$

After loading the coil heads, the yoke is installed, and the end plate and magnet shell are welded. The coils are then axially loaded to 46 kN per aperture. The loading is achieved using screws known as bullets, which push each coil with a half-moon-shaped pusher, as illustrated in Fig. 3 for the SP301 aperture, or directly against the end plate of the end cage in the SP302 aperture, as depicted in Fig. 4.

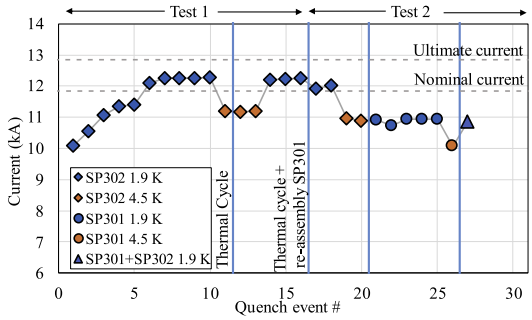

Fig. 8. Powering test results, at ramp rate 10A/s. Powering SP302, SP301 and double powering. Inominal = 11.85 kA, Iultimate = 12.85 kA.

IV. Cold Test Results

The model magnet was tested under cold conditions primarily for mechanical measurements, without specific expectations for current levels due to coil reuse. Quench locations were observed using voltage taps, and external quench heaters were used for protection, with four heaters per coil. The target current was 12.85 kA which is the ultimate current and the nominal current of the magnet is 11.85 kA.

The first test was done only in aperture SP302. As shown in Fig. 8, SP302 achieved 12.2 kA at 1.9 K, 500 A less than the previous magnet with these coils [10]. The quench location was identified in the inner layer mid-plane of coil 213, near the coil head on the non-connection side. The thermal cycle performed during the test did not affect the quench current level. At this stage, it cannot be concluded whether the observed degradation is due to the reassembly process or a consequence of the end cage implementation.

Aperture SP301 could not be tested in the first run due to insulation failure occurred between one quench heater and the coil 108. The wires of the quench heater trace and the coil voltage taps are connected in the coil head (see Fig. 3) and encapsulated with a charged epoxy adhesive. Disassembly of the magnet revealed a carbonized track across a crack in the

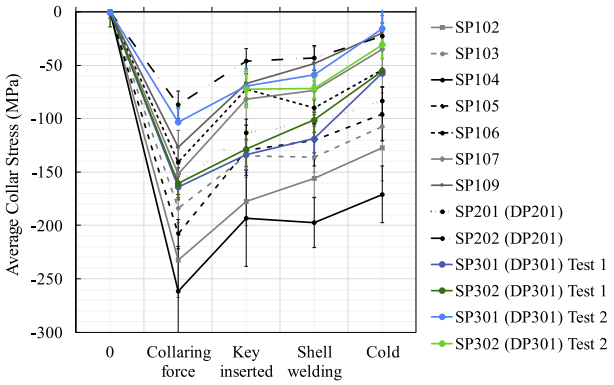

Fig. 9. Average collar nose stresses in the middle section (CM) during assembly steps and at cold.

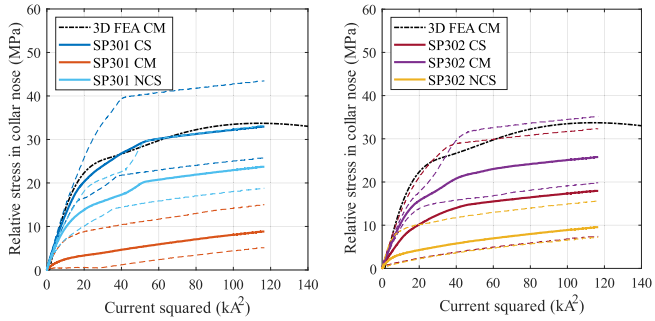

Fig. 10. Collar nose compression stress against current squared. The continuous lines represent the average of the collars section, average of four collars. The dotted lines represent the maximum and minimum measured in the collars section. The FEA represents the middle section.

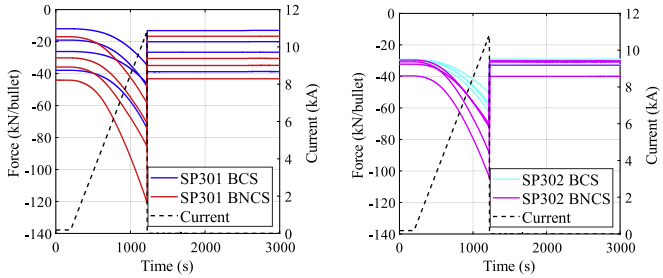

Fig. 11. Force in the bullets at cold before, during and after a quench against time in aperture SP301 (left) and SP302 (right) in the connection side (BCS) and non-connection side (BNCS).

epoxy protection. The crack, likely developed during cooldown, could have severed the wires and during the subsequent quench heater discharge tests an arc developed from the quench heater to the coil. The quench heater was replaced, and the magnet was reassembled for a second test.

In the second test, SP302 reached 12 kA at 1.9 K, 200 A less than previously, despite the collared coil was not reassembled. The quench localization was similar to the one observed before. Collared coil SP301 quenched at 10.9 kA at 1.9 K. Voltage buildup was observed in coil 108 up to 55 μV at 10 kA in the mid-plane and coil head inner layer segment, while no buildup was observed in virgin coil 214 up to 10 kA. Coil 214 did not trained. The previous magnet assembled with coil 108 reached 13.2 kA [2], suggesting a significant damage to coil 108 that likely occurred before the current assembly (e.g., when the coil was used for mechanical testing in CC999).

V. Mechanical Measurements

To represent the operating state of the magnet and achieve a balance of longitudinal forces, all mechanical measurements correspond to the current ramp of the last quench shown in Fig. 8, where both apertures reached 10.8 kA.

A. Compression Stress in the Collar Nose

Fig. 9 shows the average compressive stress in the collar nose of the central section during assembly and after cooldown for both cold tests. SP302 experienced a 56 MPa loss in prestress after the first powering test. To be comparable, the prestress in SP301 was reduced on its collaring for the test 2 (Table I and Fig. 9). The change in stress in the collar nose after cooldown is 44 MPa for both SP301 and SP302, which is higher than the average 27 MPa observed in previous 11 T model magnets. This increase is attributed to differences in the thermal shrinkage of the pole material, similar difference was obtained in a 2D FEA model.

Fig. 10 shows the stress in the collar nose during powering, with the curves shifted to zero prestress at 0 kA. The target was to have higher stress in the central area (CM) compared to the extremities (CS and NCS); this was achieved in aperture SP302 but not in SP301. The shapes of the curves during powering from the FEA results and collar strain gauges show reasonable agreement in Fig. 10. The model suggests that the observed unloading is a localized effect in the collar nose: while the center of the collar nose relaxes, the sides remain in contact with the pole. This provides a reasonable explanation for an outstanding issue concerning the interpretation of the collar nose stress measurements during powering [2].

B. Compression Force in the Magnet End Plate Bullets

After the assembly, the bullets are prestressed to -46 kN per aperture, which is the sum of the forces in the four bullets. Following cooldown, the objective is to maintain coil contact with the end plate bullets by increasing the compression. In SP301, the force per aperture increases to −95 kN on connection side and to −127 kN on the non-connection side. In SP302, the force increases to −120 kN on the connection side and −132 kN on the non-connection side. These values are lower than the FEA model's prediction of −170 kN per aperture in SP301 and −180 kN per aperture in SP302 on the connection side, likely due to frictional losses not accounted for in the model.

The delta cooldown in the magnet bullets is governed by the shrinkage of the 15 mm thick stainless-steel shell. This change is slightly larger in the aperture with the end cage, indicating stronger longitudinal support. The range of values at cold (Fig. 11) is smaller in SP302 indicating more uniform support. Fig. 11 also shows that forces fully recover after a quench in both apertures, indicating robust support memory.

During magnet energization, the bullets support the coil by absorbing longitudinal electromagnetic forces, preventing

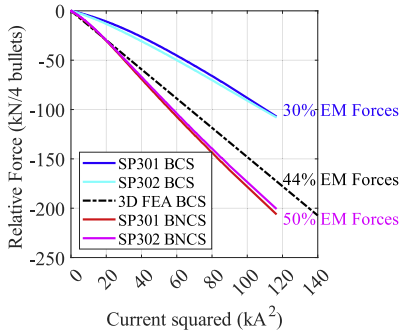

Fig. 12. Force transmitted per aperture to the bullets during powering versus current squared. Percentage of the axial electromagnetic forces at nominal current transferred to each side.

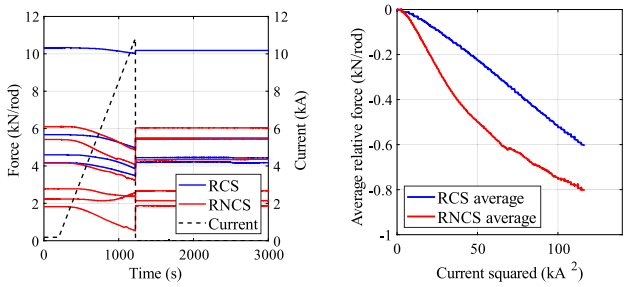

Fig. 13. End cage rods traction force at cold before, during, and after powering against time (left). Loss of force per rod shifted to zero during powering versus current squared (right). Connection side (RCS) and non-connection side (RNCS).

movement. The remaining forces are absorbed by the coil stiffness and the surrounding structure. As illustrated in Fig. 12, if the magnet had reached nominal current, 30% of the axial electromagnetic forces would have been transferred to the bullets on the connection side, while 50% to the bullets on the non-connection. The FEA model predicts that 44% of the Lorentz forces are transmitted to the bullets in connection side at nominal current. According to these experimental values, the coil head elongates by 13 µm on the connection side and by 23 µm on the non-connection side from 0 kA to 11.85 kA. As shown in (2), the forces transmitted to the connection side (CS) and non-connection side (NCS) are inversely proportional to the length of the coil head. The longer the coil head, the more forces are dissipated by the coil stiffness and the surrounding structure, resulting in fewer forces being transferred to the bullets.

$$F_{em_{bulletsNCS}} / F_{em_{bulletsCS}} = l_{headCS} / l_{headNCS} = 1.7 \tag{2}$$

After the magnet warmed up, the force in the bullets was 80% of the prestress in connection side of both apertures, 140% on the non-connection side of aperture SP301, and 110% in the non-connection side of aperture SP302. These results indicate good reproducibility of the support forces in the bullets after warming up.

C. Traction Force in the End Cage Rods in SP302

In SP302, the rods are in tension when the magnet is inserted into the cryostat for the powering test. After cooldown, the rods lose tension. The FEA predicts a decrease in force of -1.2 kN per rod. In Test 1, the strain gauges measured an average decrease of -1.7 kN per rod, and in Test 2, an average decrease of -0.8 kN per rod, which is consistent with the model prediction.

There is a significant unbalance among the different rods, as shown in the left graph of Fig. 13, with rod tensions ranging from 2 kN to 10.6 kN prior to the current ramp. There is good reproducibility in the measurements before and after a quench. The signal from two of the twelve instrumented rods on the connection side was lost after cooldown, one rod from coil 212 and one from coil 213.

During powering, the tension in the rods further decreases as the Lorentz forces push outward, causing the coil heads to be squeezed towards the outer edges of the magnet. The collar with integrated pole (Fig. 4) follows the coil winding key (Fig. 1), preventing the detachment of the outer layer first turns from the subsequent turns. According to the model, the rods are expected to experience unbalanced forces during powering of the two apertures.

At nominal current, FEA predicts an average decrease in tension of -4 ± 1 kN per rod, being higher the force transmitted to the rod closer to the magnet shell. Fig. 13(right) illustrates the average force reduction in the rods during powering, shifted to 0 kN per rod at 0 kA. Extrapolated experimental measurements at nominal current show a delta powering of -0.75 kN per rod on the non-connection side and -0.9 kN per rod on the connection side, which is more than four times smaller than the model prediction. This discrepancy may be attributed to differences in coil stiffness and friction between the real system and the model.

VI. Conclusion

This study introduced several new features on a 2-m-long 11 Tesla double-aperture model magnet to investigate reductions in high stresses in the coil heads during assembly, cooldown, and energization of the magnet and better support of the magnet ends. Mechanical measurements demonstrated that both the change in pole material and the new shimming plan reduced stresses in the coil ends during collaring and at cold, respectively. The installation of the end cage improved the homogeneity of coil longitudinal loading. At cold, aperture SP302 exhibited more uniform bullet gauge readings and better support force from the bullets compared to SP301. It was confirmed that the electromagnetic forces transfer to the bullets in connection and non-connection side are inversely proportional to the length of the coil heads. Despite the end cage maintaining tension in the rods and ensuring coil head compaction, further investigation is required to determine whether this solution is optimal for coil head support, given the inherent limitations of the coils.

Acknowledgment

The authors thank the contribution of CERN TE-MSC and EN-MME technical staff involved in the project. Special thanks to the workshop team for their precision and dedication in the magnet manufacturing.

REFERENCES

[1] G. Apollinari, I. Bejar Alonso, O. Brüning, M. Lamont, and L. Rossi, "High-luminosity large hadron collider (HL-LHC): Preliminary design," CERN Yellow Reports Monographs, 2015. [Online]. Available: https://cds.cern.ch/record/2749422

[2] S. Izquierdo Bermudez et al., "Mechanical analysis of the Nb_3Sn 11 T Dipole short models for the high luminosity LHC," *Supercond. Sci. Technol.*, vol. 32, 2019, Art. no. 085012.

[3] I. A. Santillana et al., "Advanced examination of Nb_3Sn coils and conductors for the LHC luminosity upgrade: A methodology based on computed tomography and materialographic analyses," *Supercond. Sci. Technol.*, vol. 37, no. 8, 2024, Art. no. 085007.

[4] M. Morrone and C. Garion, "Mitigation solutions on the 11 T magnet," Internal Report, 2022.

[5] P. Ebermann et al., "Irreversible degradation of Nb_3Sn Rutherford cables due to transverse compressive stress at room temperature," *Supercond. Sci. Technol.*, vol. 31, 2018, Art. no. 065009.

[6] D. Leroy, G. Spigo, A. P. Verweij, H. Boschman, R. Dubbeldam, and J. G. Pelayo, "Dipole, design and manufacture of large-bore 10 T superconducting," *IEEE Trans. Appl. Supercond.*, vol. 10, no. 1, pp. 178–182, Mar. 2000.

[7] D. Leroy et al., "Design features and performance of a 10 T twin aperture model dipole for LHC," LHC Project Rep. 176, 1998. [Online]. Available: https://www.researchgate.net/publication/42427059_Design_Features_and_Performance_of_a_10_T_Twin_Aperture_Model_Dipole_for_LHC

[8] P. Ferracin et al., "Mechanical analysis of the collaring process of the 11 T dipole magnet," *IEEE Trans. Appl. Supercond.*, vol. 29, no. 5, Aug. 2019, Art. no. 4002705.

[9] E. Nilsson et al., "Design optimization of the Nb_3Sn 11 T dipole for the high luminosity LHC," *IEEE Trans. Appl. Supercond.*, vol. 27, no. 4, Jun. 2017, Art. no. 4001005.

[10] E. Gautheron et al., "Pre-load studies on a 2-m long Nb_3Sn 11 T model magnet for the high luminosity upgrade of the LHC," *IEEE Trans. Appl. Supercond.*, vol. 31, no. 5, Aug. 2021, Art. no. 4002606.

[11] J. Ferradas Troitino et al., "Applied metrology in the production of superconducting model magnets for particle accelerators," *IEEE Trans. Appl. Supercond.*, vol. 28, no. 3, Apr. 2018, Art. no. 4002106.